Article

Elucidation of Single Hydrogen Bonds in GTPases via Experimental and Theoretical Infrared Spectroscopy

Daniel Mann,[1] Udo Höweler,[2] Carsten Kötting,[1,*] and Klaus Gerwert[1,3,*]

[1]Department of Biophysics, Ruhr University Bochum, Bochum, Germany; [2]Westfälische Wilhelms-Universität Münster, Organisch-Chemisches Institut, Münster, Germany; and [3]CAS-MPG Partner Institute for Computational Biology (PICB) Shanghai, Shanghai, China

ABSTRACT   Time-resolved Fourier transform infrared (FTIR) spectroscopy is a powerful tool to elucidate label-free the reaction mechanisms of proteins. After assignment of the absorption bands to individual groups of the protein, the order of events during the reaction mechanism can be monitored and rate constants can be obtained. Additionally, structural information is encoded into infrared spectra and can be decoded by combining the experimental data with biomolecular simulations. We have determined recently the infrared vibrations of GTP and guanosine diphosphate (GDP) bound to $G\alpha_{i1}$, a ubiquitous GTPase. These vibrations are highly sensitive for the environment of the phosphate groups and thereby for the binding mode the GTPase adopts to enable fast hydrolysis of GTP. In this study we calculated these infrared vibrations from biomolecular simulations to transfer the spectral information into a computational model that provides structural information far beyond crystal structure resolution. Conformational ensembles were generated using 15 snapshots of several 100 ns molecular-mechanics/molecular-dynamics (MM-MD) simulations, followed by quantum-mechanics/molecular-mechanics (QM/MM) minimization and normal mode analysis. In comparison with other approaches, no time-consuming QM/MM-MD simulation was necessary. We carefully benchmarked the simulation systems by deletion of single hydrogen bonds between the GTPase and GTP through several $G\alpha_{i1}$ point mutants. The missing hydrogen bonds lead to blue-shifts of the corresponding absorption bands. These band shifts for α-GTP ($G\alpha_{i1}$-T48A), γ-GTP ($G\alpha_{i1}$-R178S), and for both β-GTP/γ-GTP ($G\alpha_{i1}$-K46A, $G\alpha_{i1}$-D200E) were found in agreement in the experimental and the theoretical spectra. We applied our approach to open questions regarding $G\alpha_{i1}$: we show that the GDP state of $G\alpha_{i1}$ carries a Mg^{2+}, which is not found in x-ray structures. Further, the catalytic role of K46, a central residue of the P-loop, and the protonation state of the GTP are elucidated.

INTRODUCTION

Heterotrimeric G-proteins are ubiquitous molecular switches responsible for a variety of physiological processes such as vision, smelling, and blood pressure regulation (1–3). As with small G-proteins, their switch mechanism is maintained by surface alterations that are caused by guanosine diphosphate (GDP)-to-GTP exchange and GTP hydrolysis at the active center of the Gα subunit (4). Whereas activation is achieved via G-protein coupled receptors (GPCRs) or nonreceptor guanine nucleotide exchange factors (GEFs) (5,6), hydrolysis of GTP can be catalyzed via GTPase activating proteins (GAPs) that are called regulators of G-protein signaling (RGS) for heterotrimeric G-proteins (7). We have determined recently the individual infrared vibrations of α-, β-, and γ-GTP, α- and β-GDP, and cleaved P_i in $G\alpha_{i1}$

(8). These infrared vibrations are ultra-sensitive to environmental changes of the substrate and therefore for the binding mode the GTPase adopts to enable fast hydrolysis of GTP, which is intrinsically orders of magnitude faster than in small GTPases ($k = 0.02 \ s^{-1}$ at 15°C for $G\alpha_{i1}$ (8)). Fast hydrolysis is enabled by an intrinsic arginine finger (R178) and a catalytic glutamine (Q204) that facilitates nucleophilic attack of a water molecule at γ-GTP (4). Both critical amino acids adopt different conformations throughout different crystal structures depending on the GTP analogs used, e.g., R178 pointing away from GTP (PDB: 1GIA, 5KDL), toward β-GTP (PDB: 1TND) or toward α- and γ-GTP (PDB: 1GFI). By validation of calculated infrared (IR) spectra from quantum-mechanics/molecular-mechanics (QM/MM) calculations against the experimental values that were measured with natural GTP it will be possible to clarify the structure of the native binding pocket of $G\alpha_{i1}$ with sub-Å resolution and charge shifts that are important for catalysis can be obtained. Furthermore calculation of the inactive GDP

CrossMark

state might clarify the discussion if the inactive state of Gα_{i1} does or does not carry a Mg^{2+} ion (PDB: 1GP2, 5KDO) (9–11). There are several examples for the calculation of GTPase IR-spectra in the literature, e.g., for the small GTPases Ras (12–17), Ran (18), Arl (19), and others. We performed QM/MM calculations using several functionals (B3LYP/M06/PBEPBE) and several basis sets (6-31G*/6-311++G**). We extensively benchmarked the results against ^{18}O isotopic labeling and different Gα_{i1} point mutants that lack single hydrogen bonds toward GTP. The binding pocket of Gα_{i1} bound to Mg^{2+} and GTP after 25 ns molecular dynamics (MD) simulation is depicted in Fig. 1. We calculated and measured the point mutants Gα_{i1}-T48A that lacks a hydrogen bond toward α-GTP, Gα_{i1}-K46A that lacks hydrogen bonds toward β- and γ-GTP, Gα_{i1}-D200E that coordinates the Mg^{2+} atom via a water molecule and thereby β- and γ-GTP in the wild-type, and Gα_{i1}-R178S that lacks a hydrogen bond toward γ-GTP. Clinical relevance was previously described for the R178S mutation (20–22) as well as for T48X mutations (23). The position K46 is conserved among GTPases and ATPases (P-loop, Walker a motif) but could not be purified for intrinsic proteins so far (24). Mutation of this residue was possible in Gα_{i1} because of the tight coordination of GTP by the Ras-like and the All-Alpha domains, which now enables investigation of this crucial residue for GTPase and ATPase reaction mechanisms. Furthermore, D200 is part of the DxxG motif of GTPases. A coordination scheme of these interactions is depicted in Fig. 2 A.

MATERIALS AND METHODS

Chemicals

Para-hydroxyphenacyl(pHP)*cg*GTP and the isotopologues α-^{18}O$_2$-pHP*cg*GTP and β-^{18}O$_3$-pHP*cg*GTP, 1-(2-nitrophenyl)ethyl(NPE)cgGTP, and its isotopologue γ-^{18}O$_4$-NPE*cg*GTP were synthesized as described previously (25–28).
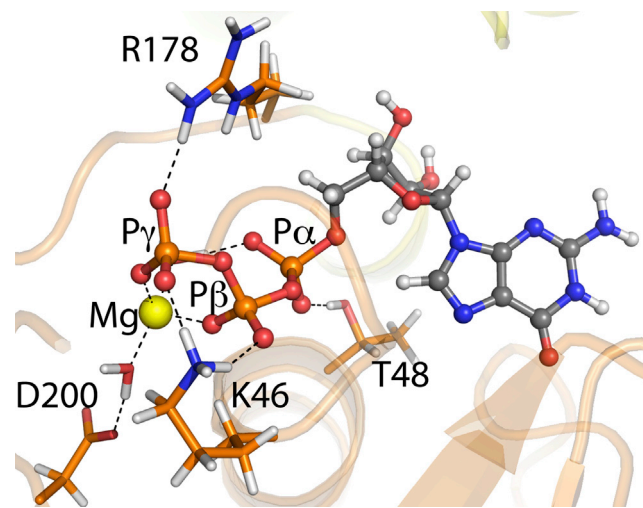

FIGURE 1 Active site of Gα_{i1} after 25 ns MD simulation. The starting structure was generated from PDB: 1GIA. To see this figure in color, go online.
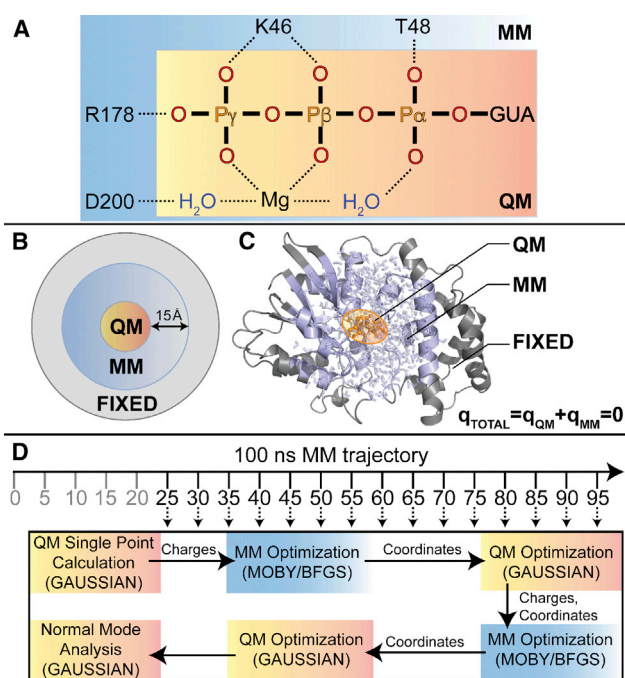

FIGURE 2 QM/MM calculation scheme. The QM box contained GTP, Mg^{2+}, and its coordinating water molecules (*A*). The QM box was embedded in a MM region that contained all protein centers and in addition all solvent atoms and ions within 1.5 nm from the nucleotide. Total charge was always zero (*B* and *C*). Fifteen snapshots of a 100 ns MM simulation were chosen as starting points for QM/MM calculations (*D*). To see this figure in color, go online.

Cloning

Human Gα_{i1} (UniProtKB P63096-1) was amplified as described previously (8). Briefly, genes were cloned into the vector pET27bmod with N-terminal 10x his-tag and tobacco etch virus (TEV) site, and transformed into *Escherichia coli* (*E. coli*) DH5α for amplification. The point mutants Gα_{i1}-R178S, Gα_{i1}-T48A, Gα_{i1}-K46A, Gα_{i1}-D200E, Gα_{i1}-D272N, and Gα_{i1}-A326S were created using the QuikChange Method (Agilent Technologies, Santa Clara, CA). Each construct was verified via sequencing.

Protein expression

The plasmid encoding wild-type or mutant Gα_{i1} was transformed into *E. coli* Rosetta2(DE3) (Novagen, Merck Millipore, Darmstadt, Germany) and incubated at 37°C overnight on lysogeny broth (LB) agar plates supplemented with 0.2% (w/v) glucose, 50 μg/mL kanamycin, and 20 μg/mL chloramphenicol. Precultures were incubated overnight at 37°C and 160 rpm in LB medium supplemented with the same components. For main cultures 6 L of LB medium supplemented with 50 μg/mL of kanamycin and 0.2% glucose were inoculated with the preculture and grown at 37°C, 100 rpm to an A$_{600}$ of 0.5 AU. Protein expression was induced at 18°C by the addition of isopropyl 1-thio-β-D-galactopyranoside (IPTG) overnight. Cells were harvested by centrifugation at 5000 g and 4°C and suspended in buffer A containing 20 mM Tris (pH 8), 300 mM NaCl, 1 mM MgCl$_2$, 0.5 mM EDTA, and 5 mM D-norleucine, flash-frozen, and stored at -80°C until protein purification.

Protein purification

Purification was performed as described (8). Briefly, cells were thawed, disrupted with a microfluidizer M-110L (Microfluidics, Newton, MA), and

centrifuged for 45 min at 45,000 g and 4°C to remove cell fragments. Supernatants were applied to a 25 mL nickel-nitrilotriacetic acid superflow column (Qiagen, Hilden, Germany) and eluted with buffers containing 200 mM imidazole. Fractions containing wild-type or mutant $G\alpha_{i1}$ were screened via SDS-PAGE, pooled, concentrated to 5 mL using a 10,000 MWCO concentrator (Amicon Ultra-15, Merck), and applied to an illustra HiLoad 26/600 Superdex 200 pg column (GE Healthcare Life Sciences, Freiburg, Germany). Peak fractions were collected, concentrated to ca. 20 mg/mL, and concentrations were determined using Bradford reagent as triplicates. Wild-type or mutant protein was aliquoted, flash-frozen in liquid nitrogen, and stored at –80°C until utilization.

Nucleotide exchange to caged GTP

Nucleotide exchange as preparation step for FTIR measurements was performed in the presence of alkaline phosphatase as described (8). Exchange rate to caged GTP was analyzed via RP-HPLC (LC-2010, Shimadzu, Kyoto, Japan) (mobile phase: 50 mM P_i (pH 6.5), 5 mM tetrabutylammoniumbromide, 7.5% acetonitrile; stationary phase: ODS-Hypersil C18 column) and was always >95% cgGTP. Samples were flash-frozen in liquid nitrogen, lyophilized-light-protected for 3 h at –55°C and 0.05 mbar in a Christ Alpha-1-2 LDPlus lyophilizer (Martin Christ GmbH, Osterode am Harz, Germany), and stored packed in parafilm and aluminum foil at –20°C until utilization.

FTIR measurements

FTIR measurements were carried out as described (8). Briefly, after background spectra were taken (400 scans), photolysis of the caged compounds was initiated with a laser flash at 308 nm with an LPX 240 XeCl excimer laser (Lambda Physics, Göttingen, Germany) (80 flashes within 160 ms) that resulted in $G\alpha_{i1}$-GTP. The subsequent hydrolysis reaction was followed in the rapid scan mode of the spectrometer at 15°C. Data were analyzed via global fit (29). The time-resolved absorbance change $\Delta A(\nu,t)$ is described by the absorbance change induced by photolysis $a_0(\nu)$ followed by a number n of exponential functions fitting the amplitudes a for each wavenumber ν. In the case of $n = 1$, a_1 corresponds to the hydrolysis spectrum. In the case of $n = 2$, a_1 corresponds to the spectrum of a conformational change of the protein, and a_2 corresponds to the following hydrolysis spectrum:

$$\Delta A(\nu, t) = a_0(\nu) + \sum_{l=1}^{n} a_l(\nu)\left(1 - e^{-k_l t}\right). \quad (1)$$

In the figures disappearing bands face downward and appearing bands face upward. Data averaged over at least three measurements. Evaluation was performed in Matlab R2012a (The MathWorks, Natick, MA) and OPUS (Bruker Corp, Billerica, MA).

Ion exchange from Mg^{2+} to Mn^{2+} at the active center of $G\alpha_{i1}$

Exchange of the bound divalent ion was performed in the presence of alkaline phosphatase similar to FTIR nucleotide exchange by digestion of the GDP nucleotide. The fast-exchange mutants $G\alpha_{i1}$-A326S (30) and $G\alpha_{i1}$-D272N (8) were chosen to enable fast equilibrium adjustment. Nucleotide exchange was performed in the presence of 50 mM $MnCl_2$ and $MgCl_2$ was also replaced by $MnCl_2$ in the FTIR buffers. Exchange rates were intrinsically analyzed by the FTIR measurements. A infrared red-shift of –8 to –10 cm^{-1} of the β-GTP band was described upon Mn^{2+} incorporation in the small GTPases Ras and Ran (18). We measured a similar red-shift of –6 cm^{-1} for the β-GTP band in both $G\alpha_{i1}$-A326S and $G\alpha_{i1}$-D272N, indicating that Mg^{2+} to Mn^{2+} exchange was performed successfully.

FTIR spectra of $G\alpha_{i1}$-WT, $G\alpha_{i1}$-A326S, and $G\alpha_{i1}$-D272N with bound Mg^{2+} were identical.

MD simulations

The structures of active $G\alpha_{i1}$-Mg^{2+}-GTPγS (PDB: 1GIA) and inactive $G\alpha_{i1}$-GDP (PDB: 1GP2) were prepared as starting structures for MD simulations in the Moby program suite (31) and simulated in the GROMACS program suite (v 4.0.7) (32–35). Structure preparation included dihedral-, angle-, and bond corrections according to the UA Amber84 force field (36). The nucleotide analogs were replaced with natural GTP or GDP. Titratable amino acids were protonated according to pKa calculations based on a generalization of the QEq-method introduced by Rappe et al. for computing partial charges (37). Their concept of charge equilibration was applied to a set of charges that were each positioned at the center of the ionizable functionality (e.g., side chain of Glu). The diagonal terms J_{AA} were set according to the pKa values of the group without interacting partners (e.g., Glu in water). The off-diagonal elements J_{AB} were calculated via a screened coulomb term. A linear regression was applied to convert the resultant "charges" to estimates of pKa values in the current structure. For example, for the direct neighbor of the arginine finger, Glu43, a local pKa of 2.25 was obtained, indicating that protonation of this group was very unlikely. The calculated local pKa of the arginine itself was higher than its reference value. Heterogroups (nucleotides, cofactors) were included in the protonation state that had been manually assigned. A full deprotonation of the phosphate groups was assigned as this was shown to be the case in the literature (38,39). For $G\alpha_{i1}$-Mg^{2+}-GDP simulations, a Mg^{2+} ion with four bound water molecules was placed next to β-GDP. The side chain of Ser47 was rotated around the Chi-1 torsion angle in a way that Mg^{2+} was coordinated by β-GDP, Ser47, and four water molecules according to the GDP-Mg^{2+} state of $G\alpha_t$ (PDB: 1TAG). Point mutations were also performed in Moby and included a short side chain optimization. Systems were initially solvated following the Vedani algorithm (40) and thoroughly solvated in a cubic simulation cell with TIP4P water (41,42) and 154 mM NaCl in GROMACS. Systems were energy minimized using the conjugate gradient method, and heated to 310 K using the Berendsen thermo- and barostat (43) with a time step of 1 fs for 25 ps with restrained protein backbone positions in the OPLS/AA force field (44). Coulomb interactions were calculated using Particle Mesh Ewald (PME; 0.9 nm) (45) and a Van der Waals (VDW) cutoff of 1.5 nm was applied. Production runs were carried out without restraints for 100 ns with a time step of 2 ps for $G\alpha_{i1}$-WT, $G\alpha_{i1}$-R178S, $G\alpha_{i1}$-T48A, $G\alpha_{i1}$-K46A, and $G\alpha_{i1}$-D200E. Replica runs were performed with different starting velocities. Evaluation was performed using the GROMACS package. Pictures were created using PyMOL (Schrödinger, Portland, OR) and Gnuplot 4.4 (46).

QM/MM calculations

QM/MM calculations were carried out using the ONIOM QM/MM embedded method (47–49) implemented in Gaussian 09 (50). The QM part contained the nucleotide (GDP or GTP), the Mg^{2+} ion, and its coordinating water molecules (Fig. 2 A). The QM area was embedded in a MM region that contained all protein centers, and in addition all solvent/ion molecules that were within a 1.5 nm shell around the QM area (Fig. 2, B and C). Total charge of the system was always zero ($q_{QM} = -2$/$q_{MM} = +2$ for $G\alpha_{i1}$-Mg^{2+}-GTP, $q_{QM} = -1$/$q_{MM} = +1$ for $G\alpha_{i1}$-Mg^{2+}-(γ-protonated-) GTP and $q_{QM} = -3$/$q_{MM} = +3$ for $G\alpha_{i1}$-GDP, and $q_{QM} = -1$/$q_{MM} = +1$ for $G\alpha_{i1}$-Mg^{2+}-GDP). This was achieved by taking Na^+/Cl^- ions into the MM region that were closest to the QM box. Several QM/MM interfaces use a plain cutoff around the QM area that determines which MM atoms are taken into account for polarization of the QM region. The amount of charges is therefore often nonzero unlike in the preceding MM-MD simulations where a neutral total charge is the prerequisite for PME treatment (51). Furthermore, as the system moves during the MM-MD simulation,

a cutoff yields different total charges that would interfere with the normal mode analysis if not corrected. We calculated the error of fluctuating charges in the calculations to be ~8 cm^{-1} (Fig. S1 in the Supporting Material). Hence we ensured that the total charge of the QM/MM systems was always zero like in the MM simulations. Charges from the Amber force field were applied for the MM part (46). We applied the quasi-Newton Broyden-Fletcher-Goldfarb-Shanno (BFGS) method (52,53) for the MM part in the external program MAXIMOBY (31). Fifteen snapshots of converged 100 ns MD simulations (starting from 25 ns) for wild-type Gα_{i1} and each point mutant were chosen as starting structures. A total energy plot of Gα_{i1}-WT is depicted in Fig. S2. Initially a single-point QM calculation was performed for the QM part (51 atoms) in the Gaussian program. QM/MM coupling was performed in the ONIOM scheme. Because the QM box contained only the nucleotide, Mg^{2+} and the coordinating water molecules the coupling only affected nonbonded interactions and no link atoms were necessary. The derived Merz-Kollman (electrostatic potential fitting, ESP) charges were transferred to the MAXIMOBY program and a BFGS minimization was performed for all substructures in the MM-part within 0.5 nm around the QM centers. Minimization was performed in the presence of all other centers in the simulation system using a cutoff of 1.5 nm for both electrostatics and Van der Waals. The MM optimization was performed using the Amber force field. In the next step, a full QM optimization was performed in the Gaussian program in the presence of the MM centers. This procedure of alternating minimizations of the QM and the MM part was performed two times, followed by IR spectra calculation using normal mode analysis (Fig. 2 D). No imaginary frequencies were observed for any calculation, indicating the QM part always reached a minimum structure. Even normal mode analysis of the MM part showed no imaginary frequencies. Calculations were performed with different functionals (B3LYP/M06/PBEPBE) (54–62) and basis sets (6-31G*/6-311++G**) (56). The functional B3LYP was chosen because it is well characterized in the literature (14,63–65). The other functionals were chosen because of their strength even for dispersion interactions (M06) and scaling factors for harmonic frequencies that are almost one (PBE). Calculated infrared frequencies were scaled according to the Computational Chemistry Comparison and Benchmark Database (CCCBDB) of the National Institute of Standards and Technology (NIST). IR frequencies were averaged over 15 snapshots for wild-type Gα_{i1} and each mutant and the standard error was calculated for comparison with the experimental bandwidths with the exception of calculations for γ-GTP protonation and geometrical exchange where only one representative structure was calculated.

RESULTS

Calculated IR spectra reproduce data from FTIR experiments

Mean values for the individual Pγ-O$_3$, Pβ-O$_2$, and Pα-O$_2$ vibrations calculated from QM/MM calculations are shown in Table 1. Depicted are only the asymmetrical stretching vibrations, because they dominate the spectrum due to their large transition dipole moment (Fig. S3) and are therefore best suited to be compared with the experimental spectrum. The

asymmetrical stretching vibrations are also the only IR frequencies that were explicitly assigned for Gα_{i1} to date (8). Atomic displacement vectors for all vibrations are depicted in Figs. S4 and S5. The Pγ-O$_3$ group showed two distinct infrared vibrations, whereas only one vibration was assessed via isotopic labeling in the experiments (8). The order of the individual phosphate vibrations was reproduced for all basis sets and functionals with the Pγ-O$_3$ vibrations giving the lowest wavenumbers, followed by the Pβ-O$_2$ and Pα-O$_2$ vibrations with higher wavenumbers. Experimental numbers (peak positions and bandwidths) were almost exactly reproduced for the functional M06, the functionals B3LYP and PBE produced IR frequencies ~20 cm^{-1} lower with the applied scaling factors. Increasing the basis set to 6-311++G** produced very similar results, indicating that the basis set 6-31G* was appropriate for the calculations. Replica QM/MM calculations of the same snapshots resulted in identical values. Calculations were also repeated for another 15 snapshots of a replica run of Gα_{i1}-WT that was performed with different starting velocities. Resulting calculated IR frequencies are depicted in Table 2. The maximum deviation between replica runs was only 5 cm^{-1} for ν_{AS}(Pβ-O$_2$) and the B3LYP functional, indicating that in both 100 ns MM production runs, similar minimum structures were reached. This also gives a deviation estimation for MM replica runs of maximal 5 cm^{-1}. The mean values of the individual phosphate vibrations and their standard deviations are compared with the experimental values and their full width at half maximum (FWHM) values in Fig. 3. A calculated IR spectrum using Gaussian functions for the bandwidths and calculated IR intensities as band heights is also depicted in Fig. S9. Because only one ν_{AS}(Pγ-O$_3$) vibration was observed experimentally, the means of the two calculated ν_{AS}(Pγ-O$_3$) vibrations were indicated as dots (Fig. 3) to enable comparison with band shifts in the following steps. This shows that the computed geometry from MM simulations (Fig. 1) is comparable with the structure of Gα_{i1} measured in FTIR experiments. This structure differs from x-ray structures, e.g., Arg178 is bound monodentately to γ-GTP in our simulations.

Elucidation of single hydrogen bonds via experimental FTIR

To benchmark our calculation scheme, we deleted single hydrogen bonds of the protein to GTP via point mutations of

TABLE 1 Mean Values of the Individual α-, β-, and γ-GTP Vibrations for Gα_{i1}-WT Calculated via QM/MM Calculations in Comparison to the Experiment (FTIR)

Vibration	FTIR (cm^{-1})	B3LYP/6-31G* (cm^{-1})	M06/6-31G* (cm^{-1})	PBE/6-31G* (cm^{-1})	B3LYP/6-311++G** (cm^{-1})	M06/6-311++G** (cm^{-1})	PBE/6-311++G** (cm^{-1})
ν_{AS}(Pγ-O$_3$)	1155	1111/1177	1126/1196	1109/1181	1110/1154	1140/1195	1110/1169
ν_{AS}(Pβ-O$_2$)	1224	1199	1222	1199	1183	1225	1186
ν_{AS}(Pα-O$_2$)	1243	1215	1245	1212	1203	1242	1203

Calculated vibrations were scaled according to CCCBCB (B3LYP/6-31G*:0.96; M06/6-31G*:0.95; PBE/6-31G*:0.99; B3LYP/6-311++G**:0.97; M06/6-311++G**:0.97; PBE/6-311++G**:1).

TABLE 2   QM/MM IR Calculations of Gα$_{i1}$-WT from a MM Replica Run

Vibration	FTIR (cm^{-1})	Replica Run			Deviation between Replica Runs		
		B3LYP/6-31G* (cm^{-1})	M06/6-31G* (cm^{-1})	PBE/6-31G* (cm^{-1})	B3LYP/6-31G* (cm^{-1})	M06/6-31G* (cm^{-1})	PBE/6-31G* (cm^{-1})
$\nu_{AS}(P\gamma\text{-}O_3)$	1155	1111/1179	1130/1196	1111/1179	0/+2	+4/0	+2/–2
$\nu_{AS}(P\beta\text{-}O_2)$	1224	1194	1220	1197	–5	–2	–2
$\nu_{AS}(P\alpha\text{-}O_2)$	1243	1211	1243	1212	–4	–2	0

Calculated vibrations were scaled according to CCCBCB (B3LYP/6-31G*:0.96; M06/6-31G*:0.95; PBE/6-31G*:0.99; B3LYP/6-311++G**:0.97; M06/6-311++G**:0.97; PBE/6-311++G**:1).

Gα$_{i1}$ and measured the proteins via FTIR spectroscopy. If the corresponding calculations match the spectral changes of these point mutations the calculation scheme is validated by a sensitive test. We created Gα$_{i1}$ point mutants of T48 that binds α-GTP, K46 that binds β- and γ-GTP, R178 that binds γ-GTP, and D200 that binds β- and γ-GTP through the Mg^{2+} ion (Fig. 2 A). The missing hydrogen bond should increase the force constant of the corresponding phosphate group that loses a hydrogen bond. An increased force constant leads to a blue-shift of the vibration. Besides the spectral information time-resolved FTIR also revealed the kinetics of the mutants. The Gα$_{i1}$-R178S and Gα$_{i1}$-K46A showed significantly slowed-down hydrolysis kinetics whereas the mutants Gα$_{i1}$-T48A and Gα$_{i1}$-D200E were only slightly slowed down (Fig. 4). Expected band shifts were also observed in the FTIR spectra as depicted in Fig. 5. The mutation Gα$_{i1}$-R178S caused a +10 cm^{-1} blue shift of the γ-GTP band only. The mutation Gα$_{i1}$-T48A caused a +27 cm^{-1} blue shift of the α-GTP band only. The mutant Gα$_{i1}$-K46A showed a blue shift of both γ-GTP (+12 cm^{-1}) and β-GTP (+10 cm^{-1}), which caused a fusion of the α-GTP and the β-GTP band. Finally, the mutant Gα$_{i1}$-D200E showed a +15 cm^{-1} blue
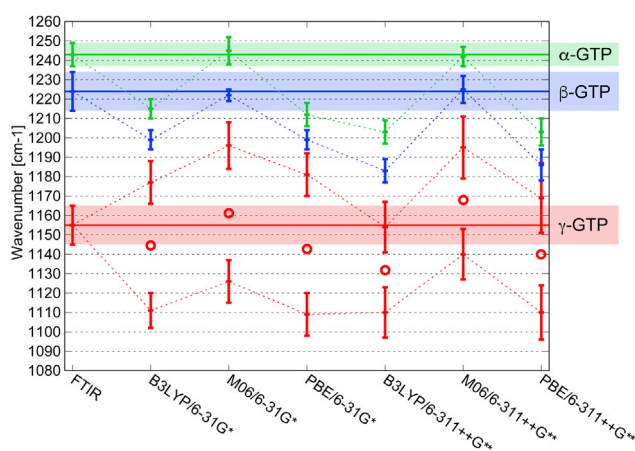

FIGURE 3   Calculated IR spectra of GTP bound to Gα$_{i1}$ with different levels of theory in comparison with experimental values (FTIR). Standard deviations (*bars*) are also depicted and compared with the FWHM values of the experiments. Mean values of the γ-GTP vibration are indicated by dots to enable comparison of band shifts with the experiments that will be discussed below. To see this figure in color, go online.
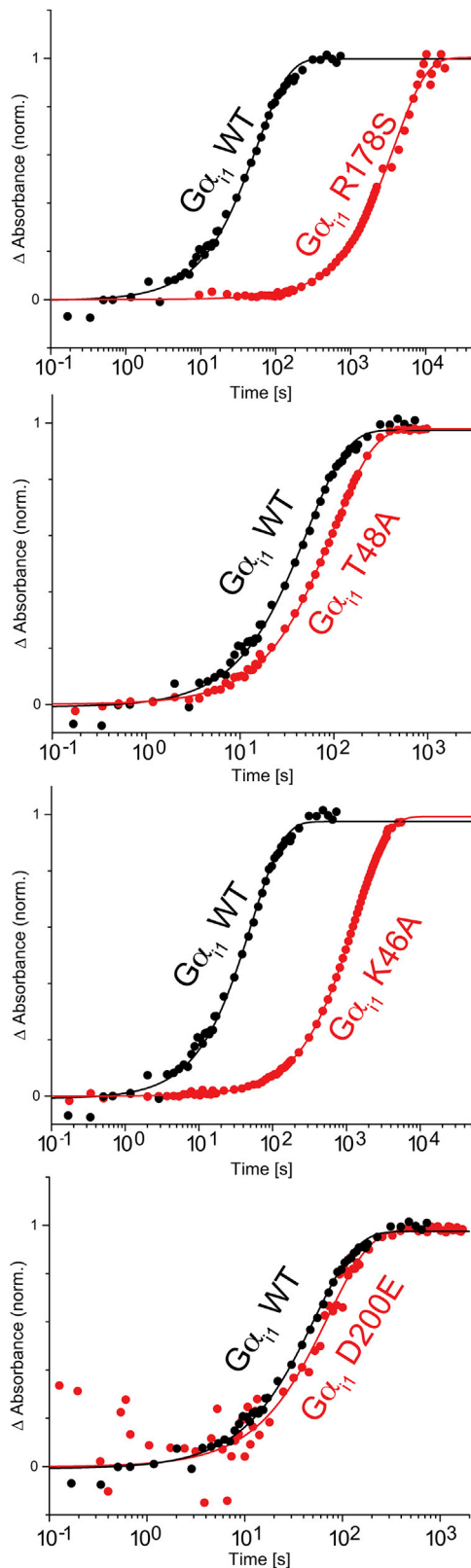
shift of γ-GTP and a –4 cm^{-1} red shift of β-GTP. All band shifts were confirmed via isotopic labeling using α-, β-, and γ-^{18}O-labeled caged GTP.

Elucidation of single hydrogen bonds via QM/MM calculations

Calculated IR band shifts of the mutants with respect to wild-type Gα$_{i1}$ are depicted in Fig. 6. Experimental FTIR band shifts (*blue*) are compared with the spectra calculated from QM/MM calculations (*red shades*) with the functionals B3LYP, M06, and PBE. The basis set was always 6-31G*. Shifts of the two γ-GTP vibrations were merged as mean values to enable a comparison with the experiment. The results of Gα$_{i1}$-R178S are in excellent agreement with the experiments. An exclusive blue-shift of the γ-GTP band was observed both in experiments and in QM/MM calculations, which again confirms that Arg178 is bound to γ-GTP. β-GTP and α-GTP show only minor shifts of 1–3 cm^{-1}, which is in agreement with the experiment. It is notable, that all surrounding amino acids including Arg178 were not treated quantum-chemically in the simulations. The mutant Gα$_{i1}$-T48A is also in good agreement with the experiments with a blue shift of the α-GTP band and minor deviations of the β-GTP band and the γ-GTP band. As shown in replica runs, the deviation between different MM-MD simulations is ~5 cm^{-1}. The mutant Gα$_{i1}$-K46A slightly differed from the experimental data. The γ-GTP shift was in good agreement, but the β-GTP blue shift exceeded the experimental shift and the α-GTP band showed a red shift of –7 to –12 cm^{-1}. However, this finding might not contradict but extend the experimental data. In FTIR experiments the mutation leads to a superposition of the α- and β-GTP bands so that only one broad absorption band was visible, which prevented precise band assignments. Isotopic labeling was not able to distinguish these vibrations whereas QM/MM calculations gave a clear band assignment. Finally, the mutant Gα$_{i1}$-D200E is also in excellent agreement with the experiment, showing a blue shift of γ-GTP and a red shift of β-GTP. Taking together the experimental and computational findings, we could on the one hand extensively verify spectra calculation from QM/MM calculations and on the other hand confirm the Gα$_{i1}$-Mg^{2+}-GTP binding model illustrated in Fig. 2 A.

FIGURE 4   Kinetics of Gα$_{i1}$ point mutants in FTIR spectroscopy at 1078 cm^{-1} (cleaved free phosphate). Points represent experimental values; lines represent the global fit. To see this figure in color, go online.

Calculation of ^{18}O isotopic labeling

In silico isotopic labeling using α-^{18}O$_2$-GTP, β-^{18}O$_3$-GTP, and γ-^{18}O$_4$-GTP was performed in the Gaussian program by modification of the atomic masses and compared with experimental FTIR measurements. The results are depicted in Fig. 7. The values for γ-, β-, and α-labeling are all in excellent agreement between experiment and theory. This demonstrates that one can obtain the band shifts upon ^{18}O labeling with high accuracy from the computational model.

Partial charge distribution explains hydrolysis-deficient Gα$_{i1}$-K46A mutant

Sums of calculated Merz-Kollman (ESP) partial charges of GTP bound to Gα$_{i1}$-WT and Gα$_{i1}$-K46A are depicted in Table 3. Mutation of Lys46 altered the charge distribution, making β-GTP more positive (+0.1 e^0). Individual ESP charges of each GTP atom are depicted in Fig. S6. It was shown (66) that GTPases transfer negative charges from γ-GTP to β-GTP toward a more product like charge distribution to facilitate GTP hydrolysis. The calculated charge distribution shows inverse behavior and thereby demonstrates why the mutation Gα$_{i1}$-K46A shows slow hydrolysis kinetics.

Experimental proof that Gα$_{i1}$-GDP carries a Mg^{2+}-ion

Mg^{2+} itself is not infrared-active but effects the vibrations of the coordinated phosphates. Thus an ion exchange to Mn^{2+} at the active center of Gα$_{i1}$ was performed and measured via FTIR spectroscopy. Exchange rates were intrinsically measured by the β-GTP shift that was previously described for small GTPases upon Mn^{2+} binding (18). A red-shift of 6 cm^{-1} was measured for both Gα$_{i1}$-D272N (Fig. 8, *black and red spectra*) and Gα$_{i1}$-A326S (Fig. S3, *black and red spectra*), indicating successful Mn^{2+} incorporation at the active center. This red-shift was even visible when the corresponding β-GTP band was labeled with ^{18}O isotopes (Fig. 8, *blue and green spectra*; Fig. S3, *blue and green spectra*) and in the hydrolysis spectra. However, not only the β-GTP band, but also the β-GDP band showed a Mn^{2+} induced red shift of 3 cm^{-1}, indicating that also the GDP state of Gα$_{i1}$ carries a Mg^{2+}/Mn^{2+} ion in our measurements (Fig. 8, *red box*). This was also the case in Gα$_{i1}$-A326S (Fig. S7, *red box*).

Proof that Gα$_{i1}$-GDP carries a Mg^{2+}-ion via QM/MM calculations

In addition to the experiments we also performed QM/MM IR spectra calculations of Gα$_{i1}$-GDP and Gα$_{i1}$-Mg^{2+}-GDP and compared them with the experimental values (Fig. S3). Fig. 9 shows that the α-GDP band does not change upon Mg^{2+} binding and is in the experimental range for both cases, independent of the functional (B3LYP/M06/PBE).
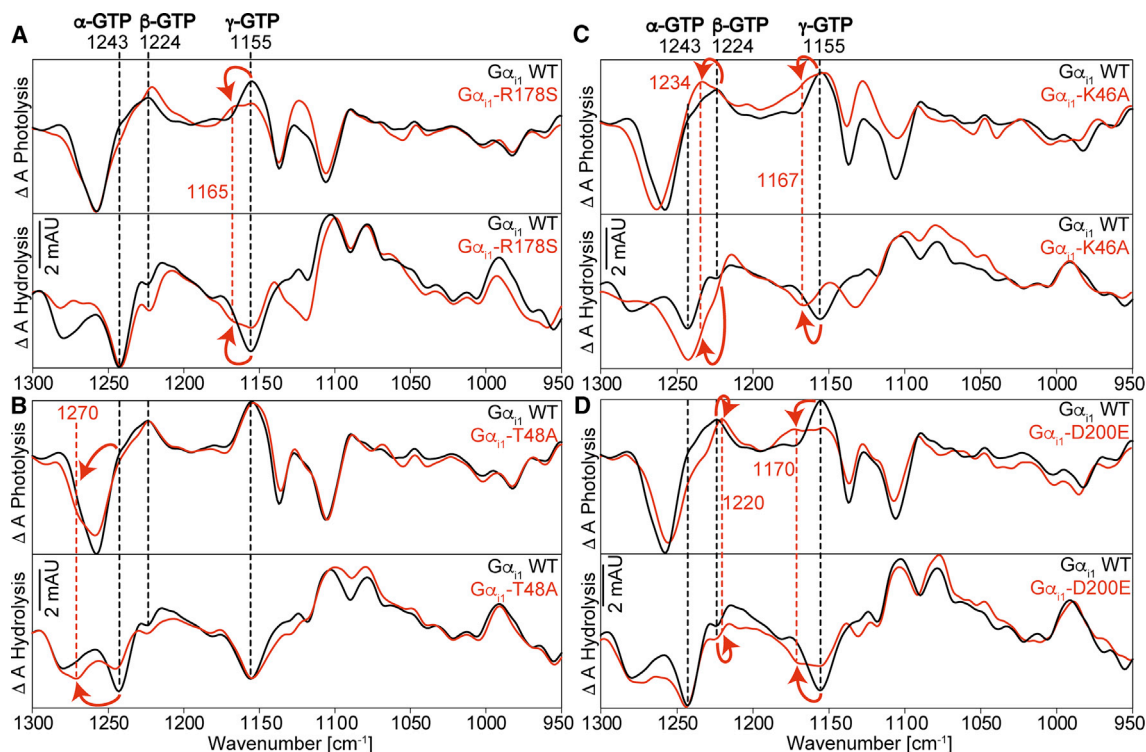
FIGURE 5 Infrared spectra of $G\alpha_{i1}$ point mutants $G\alpha_{i1}$-R178S (*A*), $G\alpha_{i1}$-T48A (*B*), $G\alpha_{i1}$-K46A (*C*) and $G\alpha_{i1}$-D200E (*D*). Photolysis and hydrolysis difference spectra of wild-type (*black*) and mutant (*red*) $G\alpha_{i1}$. Individual phosphate vibrations for α-, β-, and γ-GTP are indicated by black lines (wild-type) or red lines (mutant) and arrows. Positive bands in the photolysis spectra correspond to the $G\alpha_{i1}$-GTP state; negative bands in the photolysis spectra correspond to the $G\alpha_{i1}$-cgGTP state. Positive bands in the hydrolysis spectra correspond to the $G\alpha_{i1}$-GDP state; negative bands in the hydrolysis spectra correspond to the $G\alpha_{i1}$-GTP state. To see this figure in color, go online.

However, the values for the β-GDP vibrations significantly differ upon Mg^{2+} incorporation. The β-GDP bands are at least $+30$ cm^{-1} blue-shifted when Mg^{2+} was missing and only matched the experimental values when Mg^{2+} was bound. Therefore, a Mg^{2+} ion must be present in the inactive state of $G\alpha_{i1}$.

DISCUSSION

We have demonstrated a workflow for calculating IR spectra of GTPases from QM/MM calculations fast (within 1 day with our setup) and reproducible (maximum deviation between replica runs was 5 cm^{-1}). We considered the functional B3LYP that was extensively studied in the literature and the functionals M06 and PBE together with the basis sets 6-31G* and 6-311++G**, whereby the small basis set was sufficient to give reasonable results. We found within the error bars exact agreement between experiment and theory for the functional M06 that was able to reproduce both band peaks and bandwidths in form of standard deviations. The functionals B3LYP and PBE showed comparable results with slightly lower wavenumbers than the experiment. Calculations resulted in two distinct bands for the asymmetrical γ-GTP vibrations, one in the direction of the Mg^{2+} ion and one that included only the turned-away

oxygen atoms, whereas only one band was assigned for γ-GTP in FTIR experiments (Fig. S2) (8). However, the terminal Pγ-O$_3$ group is expected to have two asymmetrical vibrations. Accordingly, in FTIR measurements of GTP in Ras (14,56,66,67) and ATP in MsbA (68) the γ-phosphate also showed two distinct bands in isotopic labeling experiments. The same is the case for $G\alpha_{i1}$-GDP. The discrepancy between calculations and the experiment might have several reasons. First, a protonation of γ-GTP was recently suggested by neutron diffraction for the GTPase Ras (69). To check this, we parameterized protonated GTP and performed 100 ns MM-MD simulations followed by QM/MM spectra calculation for 15 snapshots (M06/6-31G*) and found large deviations not only for the γ-GTP vibrations, but also for the α- and β-GTP vibrations as depicted in Fig. S8. The upper γ-GTP band was blue-shifted $+76$ cm^{-1} above the α/β-GTP vibrations and the α- and β-GTP bands changed their order. This deviates considerably from the experiments. Therefore, a protonation of γ-GTP was most likely not the case in our experiments. These calculations also showed no imaginary frequencies. Second, a combination of the individual γ-GTP bands might occur upon geometrical exchange, e.g., by fluctuation of the Pβ-O-Pγ angle around $180°$. QM calculations showed that the angle potential of this group is very small. However,
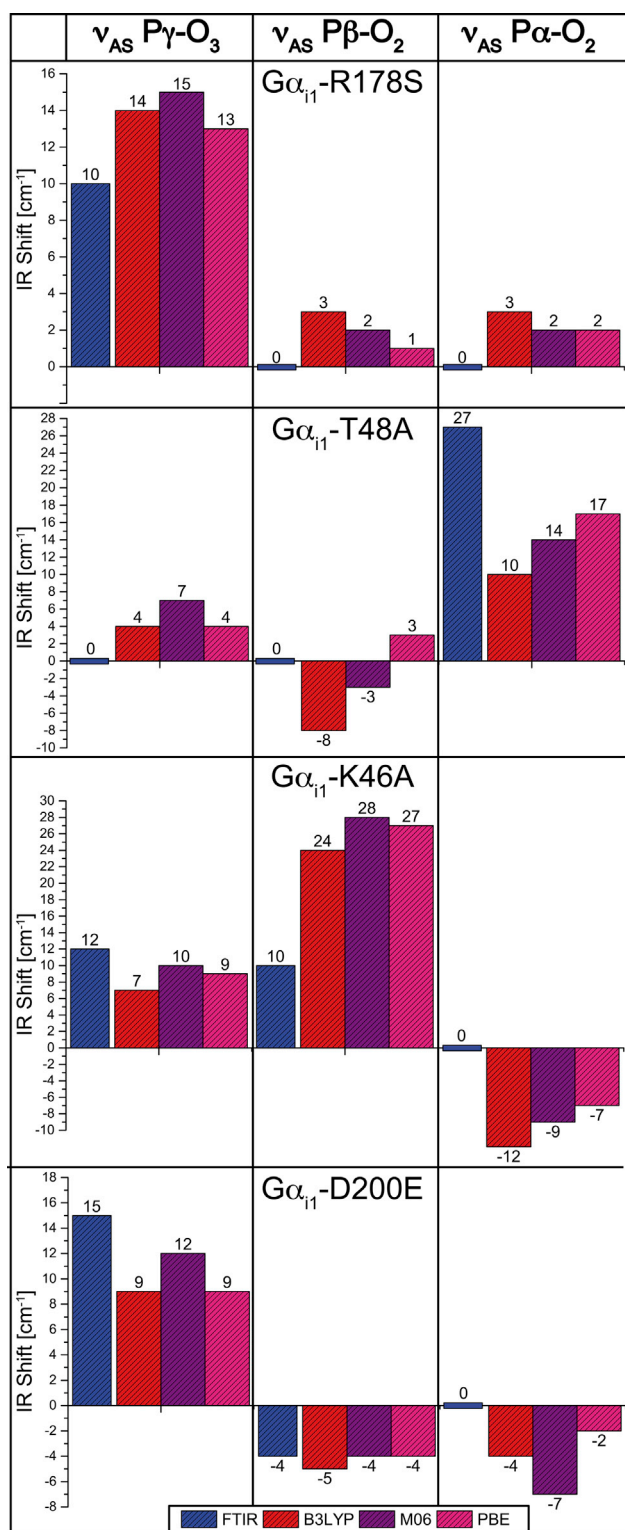
FIGURE 6 Calculated infrared absorption band shifts of $G\alpha_{i1}$ point mutants with respect to wild-type simulations. Experimental shifts are depicted in blue and calculated shifts are depicted in red shades for each individual phosphate group. To see this figure in color, go online.

the applied normal mode analysis method requires minimum structures at 0K that might differ from the experimental situation at 288K. One could solve this by a time-consuming QM/MM simulation trajectory of the system at 288K and Fourier transformation of the bond lengths. However, we consider this reason for unlikely because geometrical exchange did not occur during the performed MM-MD simulations. We also calculated the mesomeric structure with a Pβ-O-Pγ angle of nearly 180° that also resulted in two asymmetrical stretching vibrations for γ-GTP, thus such geometrical exchange did probably also not occur during the experiments. Third, water distributions around γ-GTP were highly dynamic in the MM simulations. Perhaps QM treatment of these water molecules would improve the results. Fourth, including the side chains of the Mg^{2+} coordinating amino acids in the QM box might cause a shielding of the Mg^{2+} charge that might in turn influence binding of the phosphate moieties. Fifth and most probable, the deviation between theory and experiment might be caused by the experimental methodology of FTIR difference spectroscopy. FTIR spectroscopy of GTPase reactions can only be monitored when difference spectroscopy is applied. The spectral changes that the GTPase reaction induces are three orders of magnitude smaller compared with the complete spectrum. Therefore, when educt and product bands share a similar wavelength they can add up to a zero line. The γ-GTP band at 1120 cm^{-1} is experimentally superimposed by GDP product bands (β-GDP at 1103 and 1134 cm^{-1}), impeding a clear assignment. Hence, QM/MM calculations might suggest a second γ-GTP band at 1120 cm^{-1} that is masked in the experiments because of the technique of difference spectroscopy. This is in agreement with two γ-phosphate bands for small GTPases and the ATPase MsbA (66,68). The hydrolysis spectra of $G\alpha_{i1}$-WT actually show a band at 1120 cm^{-1} that was previously not assigned (Fig. S9, indicated by asterisk; Fig. S8, dashed line). Because of negative absorptions of the pHPcg compound in this area, we also performed FTIR measurements using the different caged compound NPEcgGTP (Fig. S10) that showed intense absorptions at 1120 cm^{-1} (indicated by asterisk). This illustrates nicely how simulations and experiments can benefit from each other as this assignment would not have been possible from FTIR measurements alone.

We extensively benchmarked our calculations against $G\alpha_{i1}$ point mutants and thereby elucidated single hydrogen bonds of Arg178 toward γ-GTP, of Lys46 toward β- and γ-GTP, and of Thr48 toward α-GTP. In the FTIR experiments that affected γ-GTP, the band at 1155 cm^{-1} did not shift completely, instead a smaller band remained at this position. The same behavior was observed in ^{18}O isotopic labeling experiments when the bands were assigned (8). A smaller band that was not caused by γ-GTP lies below the γ-GTP vibration at 1155 cm^{-1}. To exclude ^{16}O exchange via back reactions we performed FTIR experiments
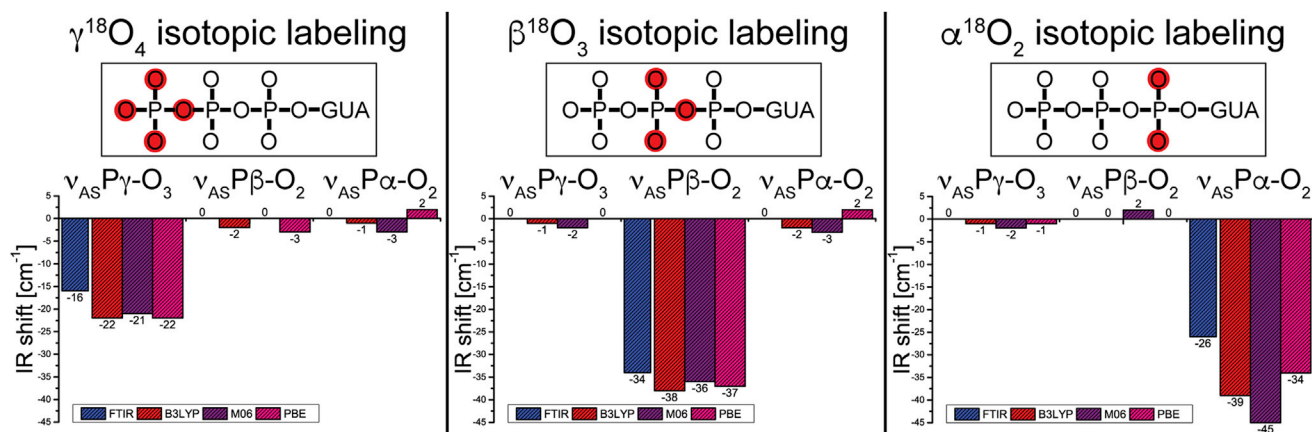
FIGURE 7 Calculated $\alpha/\beta/\gamma$ ^{18}O isotopic shifts in comparison with FTIR experiments for each individual phosphate group. ^{18}O labeled atoms are indicated in red. To see this figure in color, go online.

with $G\alpha_{i1}$-pHPcgGTP in $H_2{}^{18}O$ solvent and can exclude this effect. Changes of GTPase kinetics were also recorded during the FTIR measurements. Kinetic effects of $G\alpha_{i1}$-R178S were extensively described in the literature (20–22), whereas the mutant $G\alpha_{i1}$-K46A was only poorly characterized. Lys46, an essential residue of the P-loop and the Walker A motif, is conserved among GTPases and ATPases and often causes stability problems when mutated (24). However, nucleotide coordination in $G\alpha_{i1}$ is very tight and the mutation $G\alpha_{i1}$-K46A resulted in a functional protein. Interestingly, mutation of this residue resulted in a unification of the α- and β-GTP bands at 1245 cm^{-1}, as occurs in several wild-type ATPases, e.g., MsbA (68) (1245 cm^{-1}) and Cop-B (70) (1250 cm^{-1}). Calculation of the IR band shifts of the $G\alpha_{i1}$-K46A mutant even extended experimental findings. Because α- and β-GTP share one single infrared band in this mutation, precise determination of the individual band shifts was only possible via calculations, elucidating in addition to the blue-shift of β-GTP a Lys-induced α-GTP shift. The QM/MM calculations furthermore yielded charge distributions that might explain why the mutant $G\alpha_{i1}$-K46A is catalytically defective. ESP charges of the nucleotide resemble the charge distribution the protein experiences in the calculations. When K46 was mutated, the charge distribution was altered: the β-GTP

group was less negative ($+0.1$ e^0). Hence one role of K46 appears to be the transfer of charges toward the β-GTP group, which facilitates hydrolysis (66). The lack of this shift is expected to slow down the reaction. ESP partial charges were applied previously (71) to investigate the role of charge shifts for the catalysis of GTP hydrolysis. Because of the small QM system that included only the nucleotide and its cofactor, the ESP-fitted charges give a

TABLE 3 Charge Sums (ESP) of $G\alpha_{i1}$-WT and $G\alpha_{i1}$-K46A in QM/MM Calculations

	B3LYP/6-31G*		M06/6-31G*		PBE/6-31G*	
	$G\alpha_{i1}$-WT	$G\alpha_{i1}$-K46A	$G\alpha_{i1}$-WT	$G\alpha_{i1}$-K46A	$G\alpha_{i1}$-WT	$G\alpha_{i1}$-K46A
Σ (Pα-O$_2$)	−0.45	−0.48	−0.47	−0.47	−0.50	−0.52
$\alpha{-}\beta$ bridging O	−0.51	−0.57	−0.50	−0.57	−0.44	−0.51
Σ (Pβ-O$_2$)	−0.45	−0.37	−0.45	−0.37	−0.51	−0.42
$\beta{-}\gamma$ bridging O	−0.51	−0.57	−0.53	−0.58	−0.44	−0.51
Σ (Pγ-O$_3$)	−1.52	−1.53	−1.53	−1.54	−1.55	−1.54

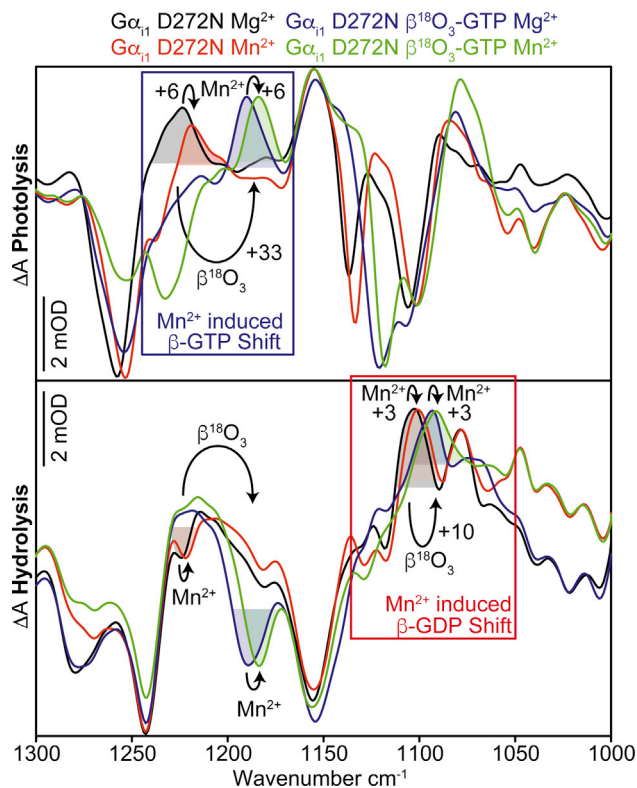Mutation of K46 makes Σ(Pβ-O$_2$) more positive, which is anticatalytic for GTP hydrolysis.

FIGURE 8 $G\alpha_{i1}$-GDP carries a Mg^{2+} ion (shown via FTIR spectroscopy). The bound Mg^{2+} ion was successfully exchanged to Mn^{2+}, which caused a red-shift of both β-GTP (*blue box*) and β-GDP (*red box*). To see this figure in color, go online.
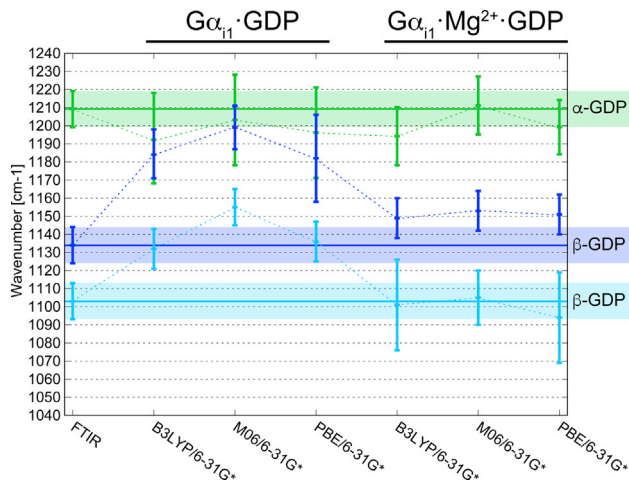
FIGURE 9   Gα$_{i1}$-GDP carries a Mg^{2+} ion (shown via QM/MM calculations). Calculations of Gα$_{i1}$-GDP did not reproduce the experimental values. When Mg^{2+} was bound to Gα$_{i1}$-GDP, the experimental values were reproduced well. Standard deviations are also depicted as bars and compared with the FWHM values of the experiment (FTIR). GDP vibrations were assigned in (8) and are shown in FTIR difference spectra in Fig. S3. To see this figure in color, go online.

good estimate of how the substrate affects the protein and vice versa.

We furthermore showed via FTIR spectroscopy and QM/MM calculations that the inactive state of Gα$_{i1}$ carries a Mg^{2+} ion, which we discussed since the x-ray structure (PDB: 1GP2) of the Gα$_{i1}$-GDP state was solved, which lacked a Mg^{2+} ion (10). Our results suggest a coordination scheme like in Gα$_t$-Mg^{2+}-GDP (PDB: 1TAG) (72). The Mn^{2+}-induced β-phosphate shift was 6 cm^{-1} for Gα$_{i1}$-GTP and 3 cm^{-1} for Gα$_{i1}$-GDP. This is in agreement with previous studies (18,73). The smaller shift of GDP compared with GTP can be explained with weaker binding of the divalent ion to GDP (total charge of −3) compared with GTP (total charge of −4). Furthermore, the influence of an exchanged divalent ion is expected to be different for a P-O$_2$ vibration as in β-GTP compared with a P-O$_3$ vibration as in β-GDP.

Finally, we demonstrated that the prediction of ^{18}O isotopic labeling is also possible with the QM/MM calculation scheme. Thus, theoretical IR spectroscopy is able to reproduce experimental spectra (Fig. S10) and extend them to high-resolved structural models.

CONCLUSIONS

Theoretical IR spectroscopy via the applied QM/MM calculation scheme is able to calculate experimental FTIR spectra of substrates bound to heterotrimeric G-proteins and translate them to an exact atomic model. We carefully benchmarked the calculations by deletion of single hydrogen bonds toward α-, β-, and γ-GTP and found good agreement between experiments and theory. The calculation of ^{18}O isotopic effects was also possible. Band shifts were reproduced for each functional (B3LYP/M06/PBE) and in addition the most recent functional M06 also reproduced experimental band positions. With this benchmark it is now possible to extend this fast theoretical approach to other GTPases and ATPases and tackle questions about geometry and catalysis like we demonstrated for the γ-GTP protonation and Mg^{2+} incorporation.

SUPPORTING MATERIAL

Ten figures are available at http://www.biophysj.org/biophysj/supplemental/S0006-3495(16)34264-3.

AUTHOR CONTRIBUTIONS

D.M. conducted the measurements. D.M. and U.H. performed the calculations. C.K. and K.G. designed the study. All authors participated in preparation of the manuscript.

ACKNOWLEDGMENTS

REFERENCES

1. Fung, B. K., J. B. Hurley, and L. Stryer. 1981. Flow of information in the light-triggered cyclic nucleotide cascade of vision. *Proc. Natl. Acad. Sci. USA.* 78:152–156.

2. May, D. C., E. M. Ross, …, M. D. Smigel. 1985. Reconstitution of catecholamine-stimulated adenylate cyclase activity using three purified proteins. *J. Biol. Chem.* 260:15829–15833.

3. Cerione, R. A., D. R. Sibley, …, R. J. Lefkowitz. 1984. Reconstitution of a hormone-sensitive adenylate cyclase system. The pure beta-adrenergic receptor and guanine nucleotide regulatory protein confer hormone responsiveness on the resolved catalytic unit. *J. Biol. Chem.* 259:9979–9982.

4. Coleman, D. E., A. M. Berghuis, …, S. R. Sprang. 1994. Structures of active conformations of Gi alpha 1 and the mechanism of GTP hydrolysis. *Science.* 265:1405–1412.

5. Rasmussen, S. G. F., B. T. DeVree, …, B. K. Kobilka. 2011. Crystal structure of the β2 adrenergic receptor-Gs protein complex. *Nature.* 477:549–555.

6. Tall, G. G., A. M. Krumins, and A. G. Gilman. 2003. Mammalian Ric-8A (synembryn) is a heterotrimeric Galpha protein guanine nucleotide exchange factor. *J. Biol. Chem.* 278:8356–8362.

7. Berman, D. M., T. M. Wilkie, and A. G. Gilman. 1996. GAIP and RGS4 are GTPase-activating proteins for the Gi subfamily of G protein alpha subunits. *Cell.* 86:445–452.

8. Schröter, G., D. Mann, …, K. Gerwert. 2015. Integration of Fourier transform infrared spectroscopy, fluorescence spectroscopy, steady-state kinetics and molecular dynamics simulations of Gαi1 distinguishes between the GTP hydrolysis and GDP release mechanism. *J. Biol. Chem.* 290:17085–17095.

9. Coleman, D. E., and S. R. Sprang. 1998. Crystal structures of the G protein Gi alpha 1 complexed with GDP and Mg2+: a crystallographic titration experiment. *Biochemistry.* 37:14376–14385.

10. Wall, M. A., D. E. Coleman, …, S. R. Sprang. 1995. The structure of the G protein heterotrimer Gi alpha 1 beta 1 gamma 2. *Cell.* 83:1047–1058.

11. Kaya, A. I., A. D. Lokits, …, H. E. Hamm. 2016. A conserved hydrophobic core in Gα_{i1} regulates G protein activation and release from activated receptor. *J. Biol. Chem.* 291:19674–19686.

12. Glennon, T. M., J. Villà, and A. Warshel. 2000. How does GAP catalyze the GTPase reaction of Ras? A computer simulation study. *Biochemistry.* 39:9641–9651.

13. Rudack, T., F. Xia, …, K. Gerwert. 2012. Ras and GTPase-activating protein (GAP) drive GTP into a precatalytic state as revealed by combining FTIR and biomolecular simulations. *Proc. Natl. Acad. Sci. USA.* 109:15295–15300.

14. Xia, F., T. Rudack, …, K. Gerwert. 2011. The specific vibrational modes of GTP in solution and bound to Ras: a detailed theoretical analysis by QM/MM simulations. *Phys. Chem. Chem. Phys.* 13:21451–21460.

15. Khrenova, M. G., B. L. Grigorenko, and A. V. Nemukhin. 2016. Theoretical vibrational spectroscopy of intermediates and the reaction mechanism of the guanosine triphosphate hydrolysis by the protein complex Ras-GAP. *Spectrochim. Acta A Mol. Biomol. Spectrosc.* 166:68–72.

16. Cavalli, A., and P. Carloni. 2002. Enzymatic GTP hydrolysis: insights from an ab initio molecular dynamics study. *J. Am. Chem. Soc.* 124:3763–3768.

17. Grigorenko, B. L., A. V. Nemukhin, …, S. K. Burt. 2005. QM/MM modeling the Ras-GAP catalyzed hydrolysis of guanosine triphosphate. *Proteins.* 60:495–503.

18. Rudack, T., S. Jenrich, …, C. Kötting. 2015. Catalysis of GTP hydrolysis by small GTPases at atomic detail by integration of x-ray crystallography, experimental, and theoretical IR spectroscopy. *J. Biol. Chem.* 290:24079–24090.

19. Khrenova, M. G., E. D. Kots, and A. V. Nemukhin. 2016. Reaction mechanism of guanosine triphosphate hydrolysis by the vision-related protein complex Arl3-RP2. *J. Phys. Chem. B.* 120:3873–3879.

20. McCune, D. J., and H. Bruch. 1937. Osterodystrophia fibrosa: report of a case in which the condition was combined with precocious puberty, pathologic pigmentation of the skin and hyperthyroidism, with a review of the literature. *Am. J. Dis. Child.* 54:806–848.

21. Albright, F., A. M. Butler, …, P. Smith. 1937. Syndrome characterized by osteitis fibrosa disseminata, areas of pigmentation and endocrine dysfunction, with precocious puberty in females: report of five cases. *N. Engl. J. Med.* 216:727–746.

22. O'Hayre, M., J. Vázquez-Prado, …, J. S. Gutkind. 2013. The emerging mutational landscape of G proteins and G-protein-coupled receptors in cancer. *Nat. Rev. Cancer.* 13:412–424.

23. Gorvin, C. M., T. Cranston, …, R. V. Thakker. 2016. A G-protein subunit-α11 loss-of-function mutation, Thr54Met, causes familial hypocalciuric hypercalcemia type 2 (FHH2). *J. Bone Miner. Res.* 31:1200–1206.

24. Du, X., and S. R. Sprang. 2009. Transition state structures and the roles of catalytic residues in GAP-facilitated GTPase of Ras as elucidated by ^{18}O kinetic isotope effects. *Biochemistry.* 48:4538–4547.

25. Gavriljuk, K., E.-M. Gazdag, …, K. Gerwert. Catalytic mechanism of a mammalian Rab·RabGAP complex in atomic detail. *Proc. Natl. Acad. Sci. USA.* 109: 21348–21353.

26. Goody, R. S. 1982. A simple and rapid method for the synthesis of nucleoside 5′-monophosphates enriched with 17O or 18O on the phosphate group. *Anal. Biochem.* 119:322–324.

27. Park, C.-H., and R. S. Givens. 1997. New photoactivated protecting groups. 6. p-hydroxyphenacyl: a phototrigger for chemical and biochemical probes. *J. Am. Chem. Soc.* 119:2453–2463.

28. Hecht, S. M., and J. W. Kozarich. 1973. A chemical synthesis of adenosine 5′-(gamma-32P)triphosphate. *Biochim. Biophys. Acta.* 331:307–309.

29. Gerwert, K. 1999. Molecular reaction mechanisms of proteins monitored by time-resolved FTIR-spectroscopy. *Biol. Chem.* 380:931–935.

30. Posner, B. A., M. B. Mixon, …, A. G. Gilman. 1998. The A326S mutant of Gialpha1 as an approximation of the receptor-bound state. *J. Biol. Chem.* 273:21752–21758.

31. Höweler, U. 2007. MAXIMOBY 11.1. CHEOPS, Altenberge, Germany.

32. Berendsen, H. J. C., D. van der Spoel, and R. van Drunen. 1995. GROMACS: a message-passing parallel molecular dynamics implementation. *Comput. Phys. Commun.* 91:43–56.

33. Lindahl, E., B. Hess, and D. van der Spoel. 2001. GROMACS 3.0: a package for molecular simulation and trajectory analysis. *Mol. Model. Annu.* 7:306–317.

34. Van Der Spoel, D., E. Lindahl, …, H. J. C. Berendsen. 2005. GROMACS: fast, flexible, and free. *J. Comput. Chem.* 26:1701–1718.

35. Pronk, S., S. Páll, …, E. Lindahl. 2013. GROMACS 4.5: a high-throughput and highly parallel open source molecular simulation toolkit. *Bioinformatics.* 29:845–854.

36. Case, D. A., V. Babin, …, P. A. Kollman. 2014. AMBER 14. University of California, San Francisco.

37. Rappe, A. K., and W. A. Goddard. 1991. Charge equilibration for molecular dynamics simulations. *J. Phys. Chem.* 95:3358–3363.

38. Schweins, T., M. Geyer, …, A. Wittinghofer. 1995. Substrate-assisted catalysis as a mechanism for GTP hydrolysis of p21ras and other GTP-binding proteins. *Nat. Struct. Biol.* 2:36–44.

39. Cheng, H., S. Sukal, …, T. S. Leyh. 2001. γ-phosphate protonation and pH-dependent unfolding of the Ras.GTP.Mg2+ complex: a vibrational spectroscopy study. *J. Biol. Chem.* 276:9931–9935.

40. Vedani, A., and D. W. Huhta. 1991. Algorithm for the systematic solvation of proteins based on the directionality of hydrogen bonds. *J. Am. Chem. Soc.* 113:5860–5862.

41. Jorgensen, W. L., J. Chandrasekhar, …, M. L. Klein. 1983. Comparison of simple potential functions for simulating liquid water. *J. Chem. Phys.* 79:926–935.

42. Horn, H. W., W. C. Swope, …, T. Head-Gordon. 2004. Development of an improved four-site water model for biomolecular simulations: TIP4P-Ew. *J. Chem. Phys.* 120:9665–9678.

43. Berendsen, H. J. C., J. P. M. Postma, …, J. R. Haak. 1984. Molecular dynamics with coupling to an external bath. *J. Chem. Phys.* 81:3684–3690.

44. Jorgensen, W. L., and J. Tirado-Rives. 1988. The OPLS [optimized potentials for liquid simulations] potential functions for proteins, energy minimizations for crystals of cyclic peptides and crambin. *J. Am. Chem. Soc.* 110:1657–1666.

45. Essmann, U., L. Perera, …, L. G. Pedersen. 1995. A smooth particle mesh Ewald method. *J. Chem. Phys.* 103:8577–8593.

46. Cornell, W. D., P. Cieplak, …, P. A. Kollman. 1996. A second generation force field for the simulation of proteins, nucleic acids, and organic molecules *J. Am. Chem. Soc.* 1995, *117*, 5179–5197. *J. Am. Chem. Soc.* 118:2309.

47. Dapprich, S., I. Komáromi, …, M. J. Frisch. 1999. A new ONIOM implementation in Gaussian98. Part I. The calculation of energies, gradients, vibrational frequencies and electric field derivatives. *J. Mol. Struct. THEOCHEM.* 461–462:1–21.

48. Vreven, T., K. Morokuma, …, M. J. Frisch. 2003. Geometry optimization with QM/MM, ONIOM, and other combined methods. I. Microiterations and constraints. *J. Comput. Chem.* 24:760–769.

49. Vreven, T., and K. Morokuma. 2006. Hybrid methods: ONIOM (QM:MM) and QM/MM. *In* Annual Reports in Computational Chemistry. Elsevier, Cambridge, MA, pp. 35–51.

50. Frisch, M. J., G. W. Trucks, …, D. J. Fox. 2009. Gaussian 09, Rev. A.02. Gaussian, Wallingford, CT.

51. Kolafa, J., and J. W. Perram. 1992. Cutoff errors in the Ewald summation formulae for point charge systems. *Mol. Simul.* 9:351–368.

52. Broyden, C. G. 1970. The convergence of a class of double-rank minimization algorithms 1. General considerations. *IMA J. Appl. Math.* 6:76–90.

53. Fletcher, R. 1970. A new approach to variable metric algorithms. *Comput. J.* 13:317–322.

54. Kim, K., and K. D. Jordan. 1994. Comparison of density functional and MP2 calculations on the water monomer and dimer. *J. Phys. Chem.* 98:10089–10094.

55. Stephens, P. J., F. J. Devlin, …, M. J. Frisch. 1994. Ab initio calculation of vibrational absorption and circular dichroism spectra using density functional force fields. *J. Phys. Chem.* 98:11623–11627.

56. Sondek, J., D. G. Lambright, …, P. B. Sigler. 1994. GTPase mechanism of Gproteins from the 1.7-A crystal structure of transducin α-GDP-AIF-4. *Nature.* 372:276–279.

57. Vosko, S. H., L. Wilk, and M. Nusair. 1980. Accurate spin-dependent electron liquid correlation energies for local spin density calculations: a critical analysis. *Can. J. Phys.* 58:1200–1211.

58. Becke, A. D. 1993. Density-functional thermochemistry. III. The role of exact exchange. *J. Chem. Phys.* 98:5648–5652.

59. Zhao, Y., and D. G. Truhlar. 2008. The M06 suite of density functionals for main group thermochemistry, thermochemical kinetics, noncovalent interactions, excited states, and transition elements: two new functionals and systematic testing of four M06-class functionals and 12 other functionals. *Theor. Chem. Acc.* 120:215–241.

60. Zhao, Y., and D. G. Truhlar. 2006. Density functional for spectroscopy: no long-range self-interaction error, good performance for Rydberg and charge-transfer states, and better performance on average than B3LYP for ground states. *J. Phys. Chem. A.* 110:13126–13130.

61. Adamo, C., and V. Barone. 1999. Toward reliable density functional methods without adjustable parameters: the PBE0 model. *J. Chem. Phys.* 110:6158–6170.

62. Perdew, J. P., K. Burke, and M. Ernzerhof. 1996. Generalized gradient approximation made simple. *Phys. Rev. Lett.* 77:3865–3868.

63. Rudack, T., F. Xia, …, K. Gerwert. 2012. The role of magnesium for geometry and charge in GTP hydrolysis, revealed by quantum mechanics/molecular mechanics simulations. *Biophys. J.* 103:293–302.

64. Nishikawa, K., J. Maruani, …, P. Piecuch. 2012. Quantum Systems in Chemistry and Physics: Progress in Methods and Applications. Springer Science, New York.

65. Lamichhane, H. P., and G. Hastings. 2011. Calculated vibrational properties of pigments in protein binding sites. *Proc. Natl. Acad. Sci. USA.* 108:10526–10531.

66. Allin, C., and K. Gerwert. 2001. Ras catalyzes GTP hydrolysis by shifting negative charges from gamma- to beta-phosphate as revealed by time-resolved FTIR difference spectroscopy. *Biochemistry.* 40:3037–3046.

67. Klähn, M., J. Schlitter, and K. Gerwert. 2005. Theoretical IR spectroscopy based on QM/MM calculations provides changes in charge distribution, bond lengths, and bond angles of the GTP ligand induced by the Ras-protein. *Biophys. J.* 88:3829–3844.

68. Syberg, F., Y. Suveyzdis, …, E. Hofmann. 2012. Time-resolved Fourier transform infrared spectroscopy of the nucleotide-binding domain from the ATP-binding Cassette transporter MsbA: ATP hydrolysis is the rate-limiting step in the catalytic cycle. *J. Biol. Chem.* 287:23923–23931.

69. Knihtila, R., G. Holzapfel, …, C. Mattos. 2015. Neutron crystal structure of RAS GTPase puts in question the protonation state of the GTP γ-phosphate. *J. Biol. Chem.* 290:31025–31036.

70. Völlmecke, C., C. Kötting, …, M. Lübben. 2009. Spectroscopic investigation of the reaction mechanism of CopB-B, the catalytic fragment from an archaeal thermophilic ATP-driven heavy metal transporter. *FEBS J.* 276:6172–6186.

71. Klähn, M., E. Rosta, and A. Warshel. 2006. On the mechanism of hydrolysis of phosphate monoesters dianions in solutions and proteins. *J. Am. Chem. Soc.* 128:15310–15323.

72. Lambright, D. G., J. P. Noel, …, P. B. Sigler. 1994. Structural determinants for activation of the α-subunit of a heterotrimeric G protein. *Nature.* 369:621–628.

73. Rohrer, M., T. F. Prisner, …, H. R. Kalbitzer. 2001. Structure of the metal-water complex in Ras x GDP studied by high-field EPR spectroscopy and ³¹P NMR spectroscopy. *Biochemistry.* 40:1884–1889.